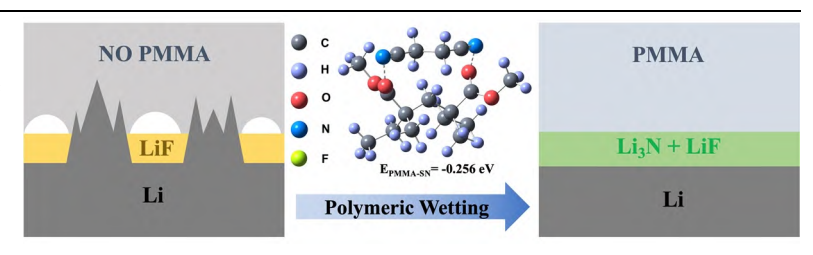


### Polymeric Wetting Matrix for a Stable Interface between Solidstate Electrolytes and Li Metal Anode

Haoran Song<sup>1</sup>, Shida Xue<sup>1</sup>, Shiming Chen<sup>1</sup>, Zijian Wang<sup>1</sup>, Yongli Song<sup>1</sup>, Jiawen Li<sup>1</sup>, Zhibo Song<sup>1</sup>, Luyi Yang<sup>1\*</sup> and Feng Pan<sup>1\*</sup>

<sup>1</sup>School of Advanced Materials, Peking University Shenzhen Graduate School, Shenzhen 518055, China

ABSTRACT Succinonitrile (SN) based solid-state electrolytes (SSEs) have potential applications in lithium (Li) batteries due to their ease of preparation and high ionic conductivity at room temperature. Here, a novel SSE consisting of poly(vinylidene fluoride-hexafluoropropylene) (PVDF-HFP), poly(methyl methacrylate) (PMMA) and Li<sub>1.3</sub>Al<sub>0.3</sub>Ti<sub>1.7</sub>(PO<sub>4</sub>)<sub>3</sub> with SN is fabricated, where PMMA is added to serve as a polymer matrix for better



wettability of SN. Due to the addition of PMMA, improved room-temperature ionic conductivity of the SSE is resulted. More importantly, better interfacial contact as well as more stable solid electrolyte interphase (SEI) layer between SSE and Li anode can be also obtained. As a result, homo- geneous and dendrite-free Li plating can be achieved for over 1000 h in Li symmetric cells. When coupled with LiNi<sub>0.5</sub>Mn<sub>0.3</sub>Co<sub>0.2</sub>O<sub>2</sub> cathode and Li anode, the proposed SSE delivers excellent cycling stability and rate capability in full-cells. By implementing SSEs with a polymeric wetting agent, this work provides fresh perspectives on stabilizing the interface between SSEs and Li metal anodes.

Keywords: Li metal, Li dendrite, poly(methyl methacrylate), succinonitrile, composite solid-state electrolyte

#### n INTRODUCTION

In recent years, lithium metal batteries (LMBs) have been widely studied in the field of energy storage.[1-4] Meanwhile, solid- state lithium metal batteries (SSLMBs) with solid-state electrolytes (SSEs) have attracted much attention because of their advantages in energy density, safety performance and simplified structure.[5-7] Exhibiting good mechanical flexibility, interfacial adaptability and facile preparation processes into thin membranes,[8,9] solid polymer electrolytes including poly(ethylene oxide) (PEO),[10-12] poly(vinylidene fluoride) (PVDF),[13-15] and poly-(acrylonitrile) (PAN)[16] have been widely studied. However, issues such as low room-temperature ionic conductivity, poor electrochemical stability and flame retardancy have hindered their practical application. [8,17] Succinonitrile (SN) is a solid plastic crystal that maintains a plastic-crystalline phase between -40 °C (transition point) and 60 °C (melting point), which means that it can remain solid state at room temperature, hence exhibiting high safety.[18] Due to the unique plastic crystalline phase, SN based polymer electrolytes possess a low flammability, high anodic oxidization potential, strong coordination ability[19,20] and ultra high ionic conductivity of more than 10<sup>-3</sup> S·cm<sup>-1</sup> at room temperature. [18] Therefore, SN is a promising electrolyte candidate for safer SSEs.

However, SN has two key problems to be solved. First, after complexation with lithium salt, it shows a lower melting point and turns into a viscous liquid-like electrolyte. [21] Researchers generally improve the mechanical strength of SN based SSE through compositing ceramic filler, [22,23] polymerization, [24,25] or the use of additional support frame. [26,27] Second, the severe side reaction between SN and Li metal affects the stability of battery. [28] Solu-

tions such as composite interlayer,<sup>[29,30]</sup> super concentrated electrolyte<sup>[28,31]</sup> and additives<sup>[26,32]</sup> have been employed to form a stable SEI. For example, Bi and coworkers<sup>[33]</sup> successfully prepared LLTO/PAN mixed nanofiber matrix by electrospinning. After absorbing SN based electrolyte, the composite membrane shows superior thermal stability and good mechanical properties. However, this preparation method has high cost and complex process, which limits its further application.

In this work, we use soft poly(vinylidene fluoride-hexafluoropropylene) (PVDF-HFP) as binder and polymer matrix to ensure the film-forming property of SSE. [34,35] Li<sub>1.3</sub>Al<sub>0.3</sub>Ti<sub>1.7</sub>(PO<sub>4</sub>)<sub>3</sub> (LATP) with low cost and good stability is used as ceramic filler to ensure the mechanical properties of SSE and inhibit the growth of lithium dendrite. [27,36] By adding poly(methyl methacrylate) (PMMA) as matrix to absorb the molten SN electrolyte, a composite SSE is prepared (denoted as PV-PM-LA-SN and the SSE without PMMA is PV-LA-SN). In addition, we found that SN can form a more stable SEI layer containing Li<sub>3</sub>N, a fast-ionic conductor, on the surface of Li metal due to the addition of PMMA, which is beneficial to uniform deposition of Li ions and interfacial stability between SN and Li. As a result, excellent electrochemical performance is achieved by PV-PM-LA-SN.

#### n RESULTS AND DISCUSSION

As shown in Figure 1a, PVDF-HFP severs as a bonding polymer matrix for LATP particles to form a dense and flexible electrolyte membrane, which contains micro-sized pores to allow SN electrolyte infiltration. By mixing SN and LiTFSI with a mass ratio of 8:1, a high ionic conductivity of SN electrolyte was prepared while maintaining its solid-state characteristics at room temperature. SN electrolyte would become liquid state with good fluidity

2205048

© 2022 fjirsm, CAS, Fuzhou

Chin. J. Struct. Chem. **2022**, 41, 2205048-2205054 DOI: 10.14102/j.cnki.0254-5861.2022-0067



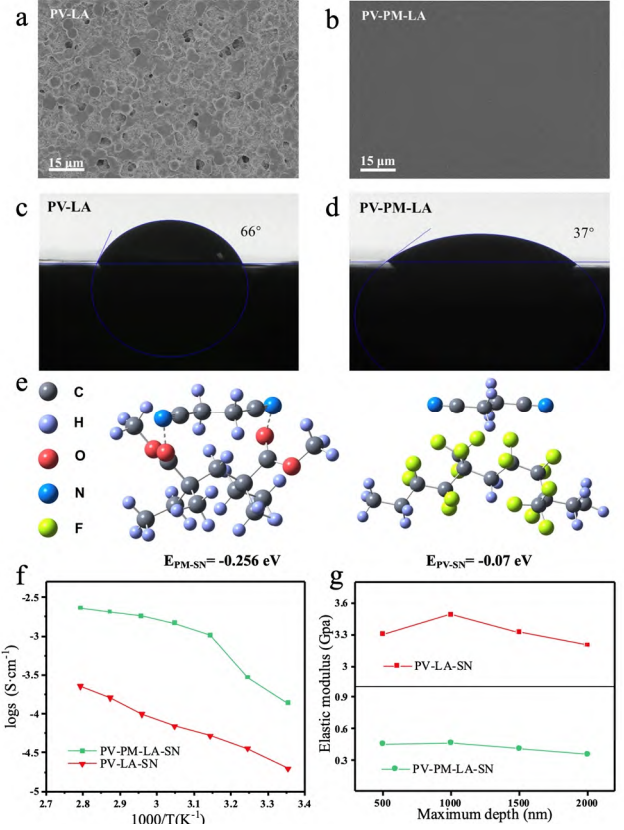


**Figure 1.** SEM image of (a) PV-LA and (b) PV-PM-LA framework. Contact angle between (c) PV-LA or (d) PV-PM-LA and SN electrolyte. (e) The corresponding DFT calculation of the interactions between SN and PMMA, PVDF-HFP. (f) Conductivity comparison of PV-LA-SN and PV-PM-LA-SN. (g) Influence of maximum depth on the elastic modulus of PV-LA-SN and PV-PM-LA-SN.

above the melting point, penetrating the pores in the framework along the surfaces. After cooling, it is recovered to solid state (Figure S1), hence the mechanical integrity and flexibility of the composite solid-state electrolyte can be well retained. However, the porous and heterogeneous surface of the composite electrolyte shown in Figure S2a suggests that SN electrolyte cannot fully fill the PV-LA framework, which could be attributed to the poor interfacial wetting between SN and PV-LA. By sharp contrast, a much smoother surface is exhibited after the introduction of PMMA (Figure S2b). This could be attributed to its ability to form a blending network with PVDF-HFP to significantly reduce the porosity of membranes (Figure 1b). More importantly, as shown in Figure 1c and 1d, the contact angle with SN decreases from ~66° (without PMMA) to ~37° (with PMMA), demonstrating the excellent compatibility between SN and PMMA.[37] Also, as shown in Figure S3, compared with pristine PVDF-HFP, PV-PM shows better swelling effect with SN. Therefore, it can be speculated that PMMA serves as a flexible sponge, which not only fills the voids in the film, but also absorbs SN for better Li-ion conduction. As is shown in Table S1, after 4 h of soaking, the mass fraction of SN in PV-PM-LA reaches a saturation value, which is about three times that of PV-LA. Density functional theory (DFT) calculations were performed to further elucidate the interaction between SN and electrolyte framework. [38-40] As shown in Figure 1e, the binding energy between SN and PMMA is calculated to be -0.256 eV, which is much higher than that between SN and PVDF-HFP (-0.07 eV), implying the greatly improved SN capture ability of PMMA.

The Arrhenius plots for ionic conductivity of both composite electrolytes are compared in Figure 1f. The ionic conductivity increases with the increase of SN content (Figure S4). After soaking for 4 h, PV-PM-LA-SN shows a room-temperature ionic conductivity of 1.38 × 10<sup>-4</sup> S·cm<sup>-1</sup>, the Li-ion conductivity of which is nearly an order of magnitude higher than that of PV-LA-SN. Although lithium transference number t (Li+) for the composite solid-state electrolytes reaches the same 0.28 (Figure S5), the better compatibility between SN and PMMA leads to this discrepancy. In PV-LA-SN, Li-ion conduction mainly depends on the mobility of SN in the porous structure of PV-LA, which is hindered by the poor interfacial wetting between SN and PV-LA. In comparison, SN can sufficiently swell PMMA, providing abundant pathways for Li-ion conduction in PV-PM-LA-SN. Moreover, the Arrhenius plot for PV-LA-SN is linear whereas PV-PM-LA-SN exhibits an inflection point, further confirming two different Li-ion conduction mechanisms.

The elastic modulus of SSE as a function of the maximum indentation depth is shown in Figure 1g. In general, measurements of the elastic modulus decrease with increasing the penetration depth. [41] The lower elastic modulus for PV-PM-LA-SN not only explains its better flexibility (Figure S6), but also suggests better interfacial contact with electrodes. In addition, the non-linear curve for PV-LA-SN membranes indicates the non-uniformity of surface, such as immiscibility of the filler and the matrix or porosity. [42] Thermogravimetric analysis (TGA) curves of PV-LA-SN and PV-PM-LA-SN are shown in Figure S7, indicating SN electrolyte and PMMA polymer which possess enough thermal stability start thermal decomposition at about 150 and 270 °C, respectively.

Since SN is unstable with Li metal, [28] Li metal anodes are pretreated by fluoroethylene carbonate (FEC) for better interfacial stability. Figure 2a shows the voltage-time profiles of the Li/Li symmetric cell in PV-PM-LA-SN and PV- LA-SN at a current density of 0.1 mA·cm<sup>-2</sup> with an areal capacity of 0.1 mAh·cm<sup>-2</sup>. The Li/PV-PM-LA-SN/Li cell cycle exhibits a lower voltage polarization of 20 mV over 500 h, whereas PV-LA-SN displays a higher polarization voltage of 90 mV, and short-circuited after 90 h. By comparing the cycling performance of PV-LA-SN and PV-SN, it is also found that the addition of LATP can effectively block the growth of lithium dendrites due to its high shear modulus (Figure S8). [43] Under an elevated current density of 0.5 mA·cm<sup>-2</sup> with an areal capacity of 0.5·mA cm<sup>-2</sup>, the Li/PV-PM-LA-SN/Li cell displays a cycle life up to 1000 h (shown in Figure 2b).

The EIS measurements show the comparison of interfacial resistance of the Li symmetric cells before and after cycling for 80 h (Figure 2c and 2d). As is shown in Figure 2c, the inset is the equivalent circuit of the EIS data.  $R_b$ ,  $R_f$ , and  $R_{ct}$  respectively represent the bulk resistance of SSE, the interfacial resistance,

Chin. J. Struct. Chem. **2022**, 41, 2205048-2205054 DOI: 10.14102/j.cnki.0254-5861.2022-0067

© 2022 fjirsm, CAS, Fuzhou

2205049

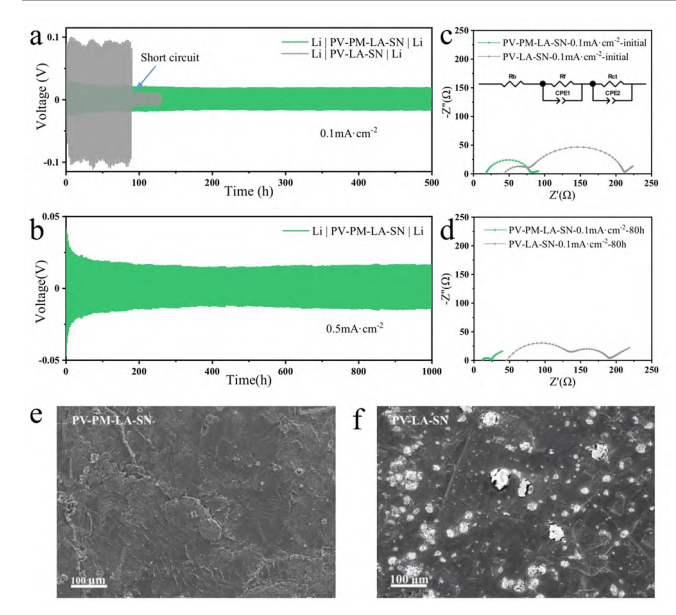


**Figure 2.** (a) The voltage-time profiles of Li symmetrical cells at a current density of 0.1 mA·cm<sup>-2</sup> with a capacity of 0.1 mAh·cm<sup>-2</sup> and (c) at a current density of 0.5 mA·cm<sup>-2</sup> with a capacity of 0.5 mAh·cm<sup>-2</sup>. (b) Nyquist plots of the Li symmetrical cells before and (d) after 80 h cycling at 0.1 mA cm<sup>-2</sup>. (e) Li anode of PV-PM-LA-SN and (f) PV-LA-SN after 80 h cycling at 0.1 mA cm<sup>-2</sup>.

and the charge transfer resistance. The Rb in Li/PV-PM-LA-SN/Li cell is initially about 18  $\Omega$ , showing a higher ionic conductivity of PV-PM-LA-SN. The initial R<sub>f</sub> and R<sub>ct</sub> for Li/PV-PM-LA-SN/Li cell are also significantly lower than that of Li/PV-LA-SN/Li, which indicates a thinner SEI and better physical contact with Li. The lower overall impedance of Li/PV-PM-LA-SN/Li cell explains its lower voltage polarization in Figure 2a. After 80 h of cycling, the R<sub>f</sub> and R<sub>ct</sub> in Li/PV-PM-LA-SN/Li cell become even lower (Table S2), suggesting improved contact between Li and SSE. The surface morphology of cycled Li anodes with PV-PM-LA-SN (Figure 2e) is much denser than that with PV-LA-SN where massive cracking can be observed. Therefore, it can be inferred that the low interfacial impedance not only lowers the overpotential, but also facilitates the uniform Li deposition, which greatly suppresses Li-dendrite formation. With the extension of cycle time, the impedance of Li/PV-PM-LA-SN/Li cell decreases gradually, while the cell using PV-LA-SN shows short circuit (Figure S9).

To further reveal the impact of PMMA on stabilizing the Lielectrolyte interface, XPS analysis was carried out for cycled cells to obtain chemical information of the SEI. Figure 3a and 3b show that for the SEI layer formed between Li and PV-PM-LA-SN, a peak corresponding to Li₃N at 398.4 can be observed, while such peak cannot be observed without PMMA. Li₃N is widely recognized as an excellent ionic conductor, which can promote the interfacial ion transfer and stabilize SEI. This can be attributed to the dipole-dipole interaction between locally negatively charged N atom of -C≡N in SN and locally positively charged C atom of -O-C=O in PMMA, which promotes the electrochemical reduction of -C≡N into Li₃N in the SEI layer. In contrast, the C≡N peak observed at 286.5 eV (Figure 3c and 3d)

represents LiCN specie resulted from the spontaneous reaction between SN and Li, which leads to unstable Li anodes. <sup>[28]</sup> As expected, a much lower amount of C≡N is observed on the Li surface in the presence of PMMA due to its inhibiting effect on the side reaction between Li and SN. In the F 1s spectra (Figure 3e and 3f), the peaks at 684.8 and 688.3 eV correspond to -CF₃ and LiF, respectively. As shown in the XPS in Figure S10, LiF is the main component of SEI on Li after pre-treatment with FEC. For PV-LA-SN, the peak intensity of LiF is weaker than that of PV-PM-LA-SN, indicating a less stable SEI. Owing to the formation of Li₃N, LiF component in the SEI for PV-PM-LA-SN is well preserved, which also contributes to the homogeneous Li plating. <sup>[47]</sup>

Figure 3g and 3h schematically illustrate the role of PMMA in SN-based SSE for Li metal batteries. On one hand, owing to the excellent infiltration between SN and PMMA, voids in the bulk and interfaces are filled, facilitating soft contact between Li and SSE. On the other hand, the addition of PMMA induces the electrochemical reduction of SN into Li<sub>3</sub>N, leading to a more stable SEI layer. Consequently, uniform Li deposition as well as better interfacial stability can be achieved simultaneously.<sup>[48]</sup>

To test the electrochemical performance of SSE in full cells, both PV-PM-LA-SN and PV-LA-SN were assembled with Li metal anode and LiNi<sub>0.5</sub>Mn<sub>0.3</sub>Co<sub>0.2</sub>O<sub>2</sub> (NMC532) cathode. Although the electrochemical window of SSE is not high enough (Figure S11), the cathode-electrolyte interphase (CEI) skin may

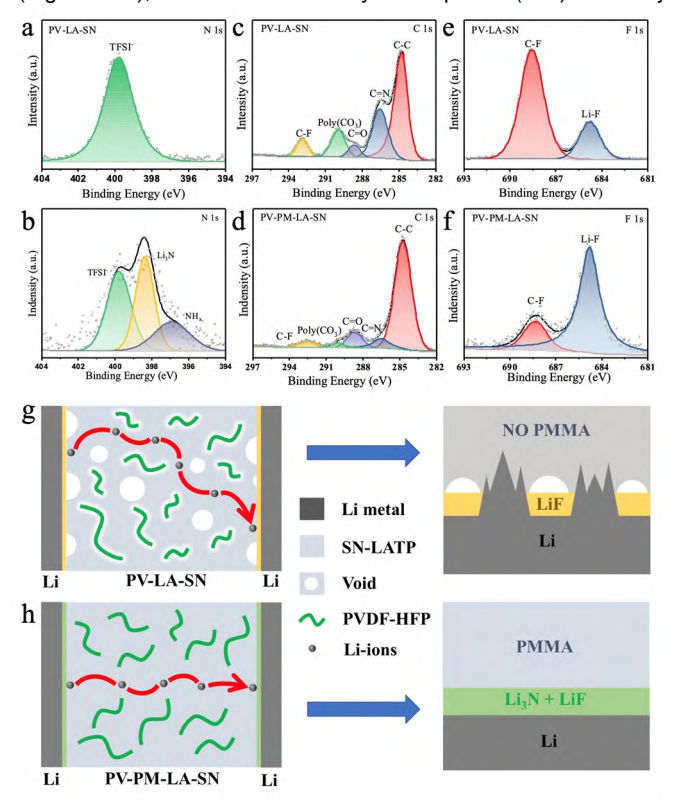


**Figure 3.** XPS of the Li metal surfaces after cycling in PV-LA-SN (a, c, e) and PV-PM-LA-SN (b, d, f). Schematic illustration of the electrochemical behavior of lithium metal anode using SSE (g) without PMMA and (h) with PMMA

2205050

© 2022 fjirsm, CAS, Fuzhou

Chin. J. Struct. Chem. **2022**, 41, 2205048-2205054 DOI: 10.14102/j.cnki.0254-5861.2022-0067



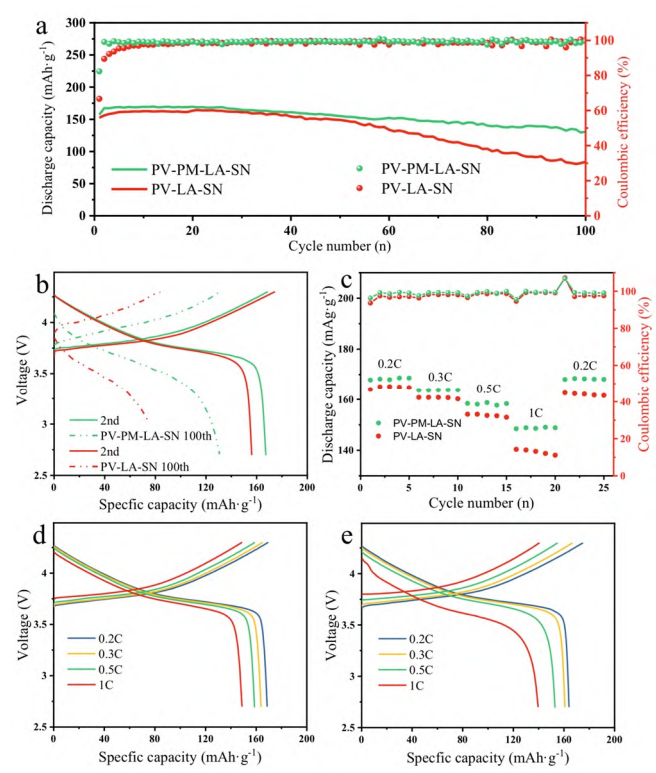


**Figure 4.** Electrochemical characterization. Cycling performance of Li/NMC532 cells. (a) Discharge capacities and Coulombic efficiency of Li/NMC532 cells at 0.2 C. (b) Voltage profiles of Li/NMC532 cells. (c) Rate capability of Li/NMC532 cells. (d) Discharge/charge curves of Li/NMC532 cells at different current densities with the PV-PM-LA-SN and (e) PV-LA-SN.

enhance the stability of cells at high voltage. Due to the better Li-electrolyte stability demonstrated above, the full cell with PV-PM-LA-SN exhibits a higher capacity retention of 77.4% compared with PV-LA-SN (50.6%) after 100 cycles at 0.2 C (Figure 4a), and the contrast becomes more obvious after 120 cycles (Figure S12). The voltage curves of the 2nd cycle and 100th cycle indicate that at the initial state of the 2nd cycle, the polarization voltage of full cell with PV-LA-SN is almost the same as PV-PM-LA-SN (Figure 4b). However, its capacity decreased rapidly and exhibited an extremely high polarization voltage at the 100th cycle. The poor capacity retention and high polarization voltage of PV-LA-SN can be attributed to the side reaction and the resulting unstable SEI. In addition, the rate capability of the two cells is shown in Figure 4c. For the full cell using PV-PM-LA-SN, the average specific capacities are 169 and 159 mAh·g<sup>-1</sup>, respectively. By contrast, the full cell using PV-LA-SN delivers lower capacities (164, 153, and 140 mAh·g<sup>-1</sup>), especially at 1 C. The greater difference at high rate can be attributed to the high Li-ion conductivity of Li<sub>3</sub>N, which further reduces the polarization voltage. However, the cell using PV-LA-SN at high rate will facilitate nonuniform Li deposition, making the interface contact worse, which can cause the changes of the average specific capacity at the rate of 0.2 C. The charge and discharge voltage-capacity curves of the full cell of PV-PM-LA-SN at different rates (Figure

4d) also exhibit lower voltage polarization compared with PV-LA-SN (Figure 4e). This result from the higher conductivity of PV-PM-LA-SN and its better interfacial contact with Li.

#### n CONCLUSION

In summary, a novel SSE (PV-PM-LA-SN) is prepared for solid-state Li metal batteries, where the PMMA serves as a sponge for absorbing SN electrolyte. Due to the addition of PMMA, the flexible composite electrolyte exhibits an improved room-temperature ionic conductivity, better interfacial contact with Li and a more stable SEI. As a result, PV-PM-LA-SN not only enables dendrite-free Li deposition with lower polarization voltage, but also delivers higher capacity retention and rate capability in full-cells. By fully utilizing the physicochemical properties of PMMA, this work provides fresh perspectives on stabilization of the interface between SSEs and Li metal anodes.

#### n EXPERIMENTAL

Preparation of PV-PM-LA-SN Electrolyte. PV-PM-LA-SN electrolyte was prepared according to the following steps: First, PVDF-HFP (MW = 0.4 M, Sigma-Aldrich), PMMA (MW = 4 M, Acros), and LATP (300 nm, MTI) were dissolved in N-methylpyrrolidone (NMP, Aladdin) at a mass ratio of 3:6:2, and then the above samples were ball-milled for 8 h. Using a 500 µm doctor blade casts the solution on the glass pane, drying it on a heating plate at 60 °C for 24 hours. After evaporation of the solvent, the membrane was stripped and punched into 19 mm diameter plates and then transferred to a vacuum oven (60 °C) for 12 hours before use. SN (Tci) electrolyte was prepared by mixing SN and LiTFSI (Aladdin) with a mass ratio of 8:1, and the mixture was heated to more than 80 °C to melt into liquid state, while about 1wt% anhydrous acetic acid was added to SN electrolyte to prevent electrolyte polymerization.<sup>[26]</sup> Then, we immerse the PV-PM-LA framework in the SN electrolyte for 4 h. After wiping and drying the excess SN electrolyte with filter papers, the PV-PM-LA-SN SSE is obtained. The preparation of PV-LA-SN and PV-SN is similar to that of PV-PM-LA-SN. All water sensitive operations are carried out in a glove box filled with argon, in which the content of H<sub>2</sub>O and O<sub>2</sub> is less than 0.1 ppm.

Preparation of Protected Lithium Anode. Li disks (15.6 mm in diameter, from China Energy Co.) were soaked into 5 mL FEC (Aladdin) for 4 hours in an Ar-filled glove box, and then dried at room temperature.

Preparation of Cathode. The cathode slurry was prepared by mixing NMC532, acetylene black and PVDF binder in NMP at a weight ratio of 8:1:1. The slurry was then applied to the carbon-coated aluminum foil with a doctor blade and dried in a vacuum oven at 80 °C for 24 h to remove the remaining solvents. Then, the cathode material was punched into disks with a diameter of 10 mm, and the active material loading was about 2 mg·cm<sup>-2</sup>.

**Electrochemical Measurements.** CR2032 coin cell was assembled in an argon filled glove box for all electrochemical tests. The full cells were tested from 2.7 to 4.3 V with NEWARE multichannel battery testing system (Shenzhen NEWARE Electronics Co., Ltd.). And five cycles of activation shall be carried out before

*Chin. J. Struct. Chem.* **2022**, 41, 2205048-2205054 DOI: 10.14102/j.cnki.0254-5861.2022-0067

© 2022 fjirsm, CAS, Fuzhou

2205051



the rate performance test. The electrochemical impedance spectroscopy (EIS) was performed in the range of  $10^6$  to 1 Hz in a Solartron 1470E electrochemical workstation (Solartron Analytical, UK). The linear sweep voltammetry (LSV) was performed in lithium/SSE/stainless steel (SS) cells at a scan rate of 0.1 mV·s<sup>-1</sup> from 3.8 to 4.8 V. Direct-current (DC) polarization with alternating current (AC) impedance in a Li/SSE/Li cell was applied to measure the lithium ion transference number t (Li<sup>+</sup>), which can be calculated with equation (1)

$$t (Li^{+}) = I_{ss}(\Delta V - I_{0}R_{1}^{0})/I_{0}(\Delta V - I_{ss}R_{1}^{ss})$$
 (1)

where  $\Delta V$  is the constant voltage applied (10 mV);  $I_0$  is the initial current;  $I_{ss}$  is the steady current;  $R_I^0$  and  $R_I^{ss}$  are the initial impedances removing the bulk resistance and steady impedances removing the bulk resistance, respectively.

Material Characterization. The ionic conductivities of electrolyte were calculated in SS symmetrical cell by the equation (2)

$$\rho = L/(R \times S) \tag{2}$$

where R is the total resistance, S the area of SSE, and L the thickness of sample.

To measure the absorption of SN, the membrane was immersed in liquid SN electrolyte for 4 h. Excess liquid was then removed from the saturated membrane. The absorbility ( $\eta$ ) can be calculated:

$$\eta = (m_1 - m_0)/m_0 \times 100\% \tag{3}$$

where  $m_0$  is the weight of the framework and  $m_1$  is the weight of composite electrolyte after reaching saturation.

Scanning electron microscopy (SEM) was used to observe the surface morphology of the lithium anode and SSE (Zeiss SU-PRA55). The X-ray photoelectron spectroscopy (XPS) was performed at a scan rate of 0.1 eV (ESCALAB 250XL). The elastic modulus of nanocomposite membranes can be determined by nanoindentation testing using a G200 Nano Indenter (Agilent Technologies). The contact angle was measured on a PT-705B dynamic system using liquid high concentration SN electrolyte under ambient condition. The water droplet volumes are 10 µL.

The thermogravimetry analysis (TGA) tests were performed with a scan range of 30-350 °C at a heating rate of 10 °C·min<sup>-1</sup> (METTLER TOLEDO).

Computational Studies. All studies were on the basis of Gaussian 09 package<sup>[38]</sup> by the DFT method. We used B3LYP<sup>[39,40]</sup> /6-311+G\*\* level to optimize the molecular structure and calculate the binding energies. The split-valence-shell Gaussian basis set 6-311+G\*\* was used for the C, H, O, N, and F atoms. We used GaussView software to calculate data and draw the schematic diagram. The binding energy ( $\Delta E_{\rm bind}$ ) was calculated to measure the binding strength of Succinonitrile (SN) and the polymer X (PVDF-HFP/PMMA). It was defined by equation (4)

$$\Delta E_{bind} = E_{SN+X} - E_{SN} - E_X + E_{BSSE}$$
 (4)

in which  $E_{\text{SN+X}}$  represents the total energy of SN/X;  $E_{\text{SN}}$  and  $E_{\text{X}}$  represent the independent energy of SN and PVDF-HFP (PMMA) respectively;  $E_{\text{BSSE}}$  is the energy of the basis set superposition error (BSSE) by the counterpoise method.

#### n ACKNOWLEDGEMENTS

This work was financially supported by National Key R&D Program of China (No. 2016YFB0700600) and Soft Science Research Project of Guangdong Province (No. 2017B030301013).

#### n AUTHOR INFORMATION

Corresponding authors. Emails: yangly@pkusz.edu.cn and panfeng@pkusz.edu.cn

#### n COMPETING INTERESTS

The authors declare no competing interests.

#### n ADDITIONAL INFORMATION

Supplementary information is available for this paper at http://manu30.magtech.com.cn/jghx/EN/10.14102/j.cnki.0254-5861.2022-0067

For submission: https://mc03.manuscriptcentral.com/cjsc

#### n REFERENCES

- (1) Jiang, P. X.; Liao, Y. F.; Liu, W.; Chen, Y. G. Alternating nanolayers as lithiophilic scaffolds for Li-metal anode. *J. Energy Chem.* **2021**, 57, 131-139.
- (2) Zhang, Q. K.; Liu, S.; Lu, Y. T.; Xing, L.; Li, W. S. Artificial interphases enable dendrite-free Li-metal anodes. *J. Energy Chem.* **2021**, 58, 198-206.
- (3) Li, S.; Li, Z.; Huai, L.; Ma, M.; Luo, K.; Chen, J.; Peng, Z. A strongly interactive adatom/substrate interface for dendrite-free and high-rate Li metal anodes. *J. Energy Chem.* **2021**, 62, 179-190.
- (4) Liu, X. H.; Qian, X. J.; Tang, W. Q.; Luo, H.; Zhao, Y.; Tan, R.; Yang, S. C.; Wu, B. Designer uniform Li plating/stripping through lithium-cobalt alloying hierarchical scaffolds for scalable high-performance lithium-metal anodes. *J. Energy Chem.* **2021**, 52, 385-392.
- (5) Jiang, Z.; Wang, S.; Chen, X.; Yang, W.; Yao, X.; Hu, X.; Wang, H. Tape-casting Li<sub>0.34</sub>La<sub>0.56</sub>TiO<sub>3</sub> ceramic electrolyte films permit high energy density of lithium-metal batteries. *Adv. Mater.* **2020**, 32, 1906221.
- (6) Han, Q.; Wang, S.; Jiang, Z.; Hu, X.; Wang, H. Composite polymer electrolyte incorporating metal-organic framework nanosheets with improved electrochemical stability for all-solid-state Li metal batteries. *ACS Appl. Mater. Interfaces* 2020, 12, 20514-20521.
- (7) Jiang, Z.; Xie, H.; Wang, S.; Song, X.; Yao, X.; Wang, H. Perovskite membranes with vertically aligned microchannels for all-solid-state lithium batteries. *Adv. Energy Mater.* **2018**, 8, 1801433.
- (8) Zuo, C.; Yang, M.; Wang, Z.; Jiang, K.; Li, S.; Luo, W.; Xue, Z. Cyclophosphazene-based hybrid polymer electrolytes obtained via epoxyamine reaction for high-performance all-solid-state lithium-ion batteries. *J. Mater. Chem. A* **2019**, 7, 18871-18879.
- (9) Wang, Z. Y.; Shen, L.; Deng, S. Q.; Cui, P.; Yao, X. Y. 10 μm-thick high-strength solid polymer electrolytes with excellent interface compatibility for flexible all-solid-state lithium-metal batteries. *Adv. Mater.* **2021**, 33, 2100353.
- (10) Liu, M.; Cheng, Z.; Ganapathy, S.; Wang, C.; Haverkate, L. A.; Tułodziecki, M.; Wagemaker, M. Tandem interface and bulk Li-ion transport in a hybrid solid electrolyte with microsized active filler. *ACS Energy Lett.* **2019**, 4, 2336-2342.
- (11) Song, Y. L.; Yang, L. Y.; Li, J. W.; Zhang, M.; Wang, Y.; Li, S.; Pan, F. Synergistic dissociation-and-trapping effect to promote Li-ion conduction in polymer electrolytes via oxygen vacancies. *Small* **2021**, 17, 2102039.

2205052

© 2022 fjirsm, CAS, Fuzhou

Chin. J. Struct. Chem. **2022**, 41, 2205048-2205054 DOI: 10.14102/j.cnki.0254-5861.2022-0067



- (12) Wang, Z. J.; Yang, L. Y.; Liu, J. J.; Song, Y. L.; Zhao, Q. H.; Yang, K.; Pan, F. Tuning rate-limiting factors to achieve ultrahigh-rate solid-state sodium-ion batteries. *ACS Appl. Mater. Interfaces* **2020**, 12, 48677-48683.
- (13) Liu, L.; Zhang, D.; Zhao, J.; Shen, J.; Li, F.; Yang, Y.; Liu, J. Synergistic effect of lithium salts with fillers and solvents in composite electrolytes for superior room-temperature solid-state lithium batteries. *ACS Appl. Energy Mater.* **2022**, 5, 2484-2494.
- (14) Wang, Z. J.; Yang, K.; Song, Y. L.; Lin, H.; Li, K.; Cui, Y.; Yang, L. Y.; Pan, F. Polymer matrix mediated solvation of LiNO<sub>3</sub> in carbonate electrolytes for quasi-solid high-voltage lithium metal batteries. *Nano Res.* **2020**, 13, 2431-2437.
- (15) Wang, Z. Y.; Guo, Q. Y.; Jiang, R. G.; Deng, S. G.; Ma, J. F.; Cui, P.; Yao, X. Y. Porous poly (vinylidene fluoride) supported three-dimensional poly (ethylene glycol) thin solid polymer electrolyte for flexible high temperature all-solid-state lithium metal batteries. *Chem. Eng. J.* **2022**, 435, 135106
- (16) Tamilarasan, P.; Ramaprabhu, S. Graphene based all-solid-state supercapacitors with ionic liquid incorporated polyacrylonitrile electrolyte. *Energy* **2013**, 51, 374-381.
- (17) Zhu, P.; Yan, C.; Dirican, M.; Zhu, J.; Zang, J.; Selvan, R. K.; Zhang, X. Li<sub>0.33</sub>La<sub>0.557</sub>TiO<sub>3</sub> ceramic nanofiber-enhanced polyethylene oxide-based composite polymer electrolytes for all-solid-state lithium batteries. *J. Mater. Chem. A* **2018**, 6, 4279-4285.
- (18) Alarco, P. J.; Abu-Lebdeh, Y.; Abouimrane, A.; Armand, M. The plastic-crystalline phase of succinonitrile as a universal matrix for solid-state ionic conductors. *Nat. Mater.* **2004**, 3, 476-481.
- (19) Hu, P.; Chai, J.; Duan, Y.; Liu, Z.; Cui, G.; Chen, L. Progress in nitrile-based polymer electrolytes for high performance lithium batteries. *J. Mater. Chem. A* **2016**, 4, 10070-10083.
- (20) Yang, Y. N.; Jiang, F. L.; Li, Y. Q.; Wang, Z. X.; Zhang, T. A surface coordination interphase stabilizes a solid-state battery. *Angew. Chem. Int. Ed.* **2021**, 60, 24162-24170.
- (21) Das, S.; Prathapa, S. J.; Menezes, P. V.; Row, T. N. G.; Bhattacharyya, A. J. Study of ion transport in lithium perchlorate-succinonitrile plastic crystalline electrolyte via ionic conductivity and in situ cryocrystallography. *J. Phys. Chem. B* **2009**, 113, 5025-5031.
- (22) Kwon, T.; Choi, I.; Park, M. J. Highly conductive solid-state hybrid electrolytes operating at subzero temperatures. *ACS Appl. Mater. Interfaces* **2017**, 9, 24250-24258.
- (23) Liu, L.; Cai, Y.; Zhao, Z.; Ma, C.; Li, C.; Mu, D. A succinonitrile-infiltrated silica aerogel synergistically-reinforced hybrid solid electrolyte for durable solid-state lithium metal batteries. *Mater. Chem. Front.* **2022**, 6, 430-439.
- (24) Zheng, T.; Cui, X.; Chu, Y.; Li, H.; Pan, Q. Ultrahigh elastic polymer electrolytes for solid-state lithium batteries with robust interfaces. *ACS Appl. Mater. Interfaces* **2022**, 14, 5932-5939.
- (25) Lee, M. J.; Han, J.; Lee, K.; Lee, Y. J.; Kim, B. G.; Jung, K. N.; Lee, S. W. Elastomeric electrolytes for high-energy solid-state lithium batteries. *Nature* **2022**, 601, 217-222.
- (26) Jiang, T.; He, P.; Wang, G.; Shen, Y.; Nan, C. W.; Fan, L. Z. Solvent-free synthesis of thin, flexible, nonflammable garnet-based composite solid electrolyte for all-solid-state lithium batteries. *Adv. Energy Mater.* **2020**, 10, 1903376.
- (27) Gai, J.; Ma, F.; Zhang, Z.; Sun, D.; Jin, Y.; Guo, Y.; Kim, W. Flexible organic-inorganic composite solid electrolyte with asymmetric structure for room temperature solid-state Li-ion batteries. ACS Sustain. Chem.

Eng. 2019, 7, 15896-15903.

- (28) Yamada, Y.; Furukawa, K.; Sodeyama, K.; Kikuchi, K.; Yaegashi, M.; Tateyama, Y.; Yamada, A. Unusual stability of acetonitrile-based superconcentrated electrolytes for fast-charging lithium-ion batteries. *J. Am. Chem. Soc.* **2014**, 136, 5039-5046.
- (29) Hao, S.; Li, L.; Cheng, W.; Ran, Q.; Ji, Y.; Wu, Y.; Liu, X. Long-chain fluorocarbon driven hybrid solid polymer electrolyte for lithium metal battery. *J. Mater. Chem. A* 2022, 10, 4881-4888.
- (30) Yue, H.; Li, J.; Wang, Q.; Li, C.; Zhang, J.; Li, Q.; Yang, S. Sandwich-like poly(propylene carbonate)-based electrolyte for ambient-temperature solid-state lithium ion batteries. *ACS Sustain. Chem. Eng.* **2018**, 6, 268-274
- (31) Zha, W.; Li, J.; Li, W.; Sun, C.; Wen, Z. Anchoring succinonitrile by solvent-Li<sup>+</sup> associations for high-performance solid-state lithium battery. *Chem. Eng. J.* **2021**, 406, 126754.
- (32) Wang, C.; Adair, K. R.; Liang, J.; Li, X.; Sun, Y.; Li, X.; Sun, X. Solid-state plastic crystal electrolytes: effective protection interlayers for sulfide-based all-solid-state lithium metal batteries. *Adv. Funct. Mater.* **2019**, 29, 1900392
- (33) Bi, J.; Mu, D.; Wu, B.; Fu, J.; Yang, H.; Mu, G.; Wu, F. A hybrid solid electrolyte Li<sub>0.33</sub>La<sub>0.557</sub>TiO<sub>3</sub>/poly(acylonitrile) membrane infiltrated with a succinonitrile-based electrolyte for solid state lithium-ion batteries. *J. Mater. Chem. A* **2020**, 8, 706-713.
- (34) Wei, T.; Zhang, Z. H.; Wang, Z. M.; Zhang, Q.; Ye, Y. S.; Lu, J. H.; Zhang, Z. W. Ultrathin solid composite electrolyte based on Li<sub>6.4</sub>La<sub>3</sub>Zr<sub>1.4</sub>Ta<sub>0.6</sub>O<sub>12</sub>/PVDF-HFP/LiTFSI/succinonitrile for high-performance solid-state lithium metal batteries. *ACS Appl. Energy Mater.* **2020**, 3, 9428-9435.
- (35) Xu, F. L.; Deng, S. G.; Guo, Q. Y.; Zhou, D.; Yao, X. Y. Quasi-ionic liquid enabling single-phase poly (vinylidene fluoride)-based polymer electrolytes for solid-state LiNi<sub>0.6</sub>Co<sub>0.2</sub>Mn<sub>0.2</sub>O<sub>2</sub>||Li batteries with rigid-flexible coupling interphase. *Small Methods* **2021**, 5, 2100262.
- (36) Chen, H.; Zhou, C. J.; Dong, X. R.; Yan, M.; Liang, J. Y.; Xin, S.; Zeng, X. X. Revealing the superiority of fast ion conductor in composite electrolyte for dendrite-free lithium-metal batteries. *ACS Appl. Mater. Interfaces* **2021**, 13, 22978-22986.
- (37) Zha, W.; Li, W.; Ruan, Y.; Wang, J.; Wen, Z. In situ fabricated ceramic/polymer hybrid electrolyte with vertically aligned structure for solid-state lithium batteries. *Energy Storage Mater.* **2021**, 36, 171-178.
- (38) Frisch, G. W.; Trucks, H. B.; Schlegel, G. E.; Scuseria, M. A.; Robb, J. R.; Cheeseman, G.; Scalmani, V.; Barone, G. A.; Petersson, H.; Nakatsuji, X.; Li, M.; Caricato, A.; Marenich, J.; Bloino, B. G.; Janesko, R.; Gomperts, B.; Mennucci, H. P.; Hratchian, J. V.; Ortiz, A. F.; Izmaylov, J. L.; Sonnenberg, D.; Williams-Young, F.; Ding, F.; Lipparini, F.; Egidi, J.; Goings, B.; Peng, A.; Petrone, T.; Henderson, D.; Ranasinghe, V. G.; Zakrzewski, J.; Gao, N.; Rega, G.; Zheng, W.; Liang, M.; Hada, M.; Ehara, K.; Toyota, R.; Fukuda, J.; Hasegawa, M.; Ishida, T.; Nakajima, Y.; Honda, O.; Kitao, H.; Nakai, T.; Vreven, K.; Throssell, J. A.; Montgomery, Jr. J. E.; Peralta, F.; Ogliaro, M.; Bearpark, J. J.; Heyd, E.; Brothers, K. N.; Kudin, V. N.; Staroverov, T.; Keith, R.; Kobayashi, J.; Normand, K.; Raghavachari, A.; Rendell, J. C.; Burant, S. S.; Iyengar, J.; Tomasi, M.; Cossi, J. M.; Millam, M.; Klene, C.; Adamo, R.; Cammi, J. W.; Ochterski, R. L.; Martin, K.; Morokuma, O.; Farkas, J. B.; Foresman, D. J. Fox, Gaussian 09, Revision A. 02, M. J. Gaussian, Inc., Wallingford CT 2016.
- (39) Becke, A. Density-functional thermochemistry. III. The role of exact exchange. *J. Chem. Phys.* **1998**, 98, 5648-5652.

*Chin. J. Struct. Chem.* **2022**, 41, 2205048-2205054 DOI: 10.14102/j.cnki.0254-5861.2022-0067

© 2022 fjirsm, CAS, Fuzhou

2205053

#### **ARTICLE**



- (40) Lee, C.; Yang, W.; Parr, R. G. Development of the Colle-Salvetti correlation-energy into a function of the electron density. *Phys. Rev.* **1998**, 37, 785-788.
- (41) Zhao, M.; Slaughter, W. S.; Li, M.; Mao, S. X. Material-length-scale-controlled nanoindentation size effects due to strain-gradient plasticity. *Acta Mater.* **2003**, 51, 4461-4469.
- (42) Liu, Y.; Sun, Y.; Zeng, F.; Liu, J.; Ge, J. Effect of POSS nanofiller on structure, thermal and mechanical properties of PVDF matrix. *J. Nanopart. Res.* **2013**, 15, 1-10.
- (43) Yang, L. Y.; Wang, Z. J.; Feng, Y.; Tan, R.; Zuo, Y.; Gao, R.; Pan, F. Flexible composite solid electrolyte facilitating highly stable "soft contacting" Li-electrolyte interface for solid state lithium-ion batteries. *Adv. Energy Mater.* **2017**, 7, 1701437.
- (44) Eshetu, G. G.; Judez, X.; Li, C.; Bondarchuk, O.; Rodriguez-Martinez, L. M.; Zhang, H.; Armand, M. Lithium azide as an electrolyte additive for all-solid-state lithium-sulfur batteries. *Angew. Chem. Int. Ed.* **2017**, 56, 15368-15372.
- (45) Wang, C.; Sun, X.; Yang, L.; Song, D.; Wu, Y.; Ohsaka, T.; Wu, J. In situ ion-conducting protective layer strategy to stable lithium metal anode

for all-solid-state sulfide-based lithium metal batteries. Adv. Mater. Interfaces 2021, 8, 2001698.

- (46) Choi, J.; Zabihi, O.; Varley, R. J.; Fox, B.; Naebe, M. Enhancement of ionic conduction and mechanical properties for all-solid-state polymer electrolyte systems through ionic and physical bonding. *Mater. Today Chem.* **2022**, 23, 100663.
- (47) Chen, T.; Kong, W.; Zhang, Z.; Wang, L.; Hu, Y.; Zhu, G.; Jin, Z. Ionic liquid-immobilized polymer gel electrolyte with self-healing capability, high ionic conductivity and heat resistance for dendrite-free lithium metal batteries. *Nano Energy* 2018, 54, 17-25.
- (48) Zhang, Q.; Liu, K.; Ding, F.; Li, W.; Liu, X.; Zhang, J. Enhancing the high voltage interface compatibility of LiNi<sub>0.5</sub>Co<sub>0.2</sub>Mn<sub>0.3</sub>O<sub>2</sub> in the succinonitrile-based electrolyte. *Electrochim. Acta* **2019**, 298, 818-826.

Received: March 22, 2022 Accepted: April 21, 2022 Published: May 20, 2022



### Polymeric Wetting Matrix for a Stable Interface between Solidstate Electrolytes and Li Metal Anode

Haoran Song<sup>1</sup>, Shida Xue<sup>1</sup>, Shiming Chen<sup>1</sup>, Zijian Wang<sup>1</sup>, Yongli Song<sup>1</sup>, Jiawen Li<sup>1</sup>, Zhibo Song<sup>1</sup>, Luyi Yang<sup>1\*</sup> and Feng Pan<sup>1\*</sup>

<sup>1</sup> School of Advanced Materials, Peking University Shenzhen Graduate School, Shenzhen 518055, China Corresponding authors. Email: yangly@pkusz.edu.cn; panfeng@pkusz.edu.cn



Table S1. Variation of Succinonitrile Content with Infiltration Time

Inliltration	PV-PM-LA	PV-LA
1h	20	11
2h	31	13.5
3h	33	13.5
4h	37	13.5
5h	37	13.5
6h	37	13.5



 $\textbf{Table \underline{S2.}} \ \text{Impedance Information } R_{\text{ct}} \ \text{before and after Cycling}$ 

Cycling	PV-PM-LA-SN	PV-LA-SN
before	38.2	138.7
after	0.9	69.8





Figure S1. Photographs of SN electrolyte at 25°C.



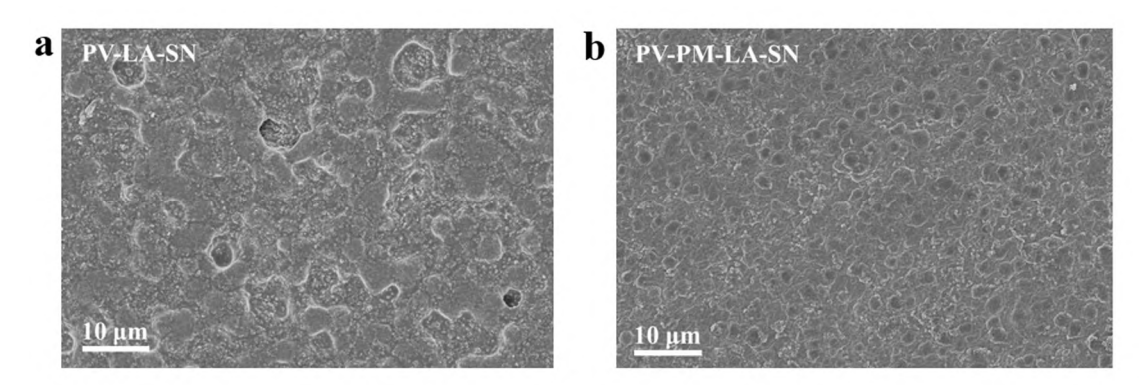


Figure S2. Scanning electron microscopy image of (a) PV-LA-SN and (b) PV-PM-LA-SN.



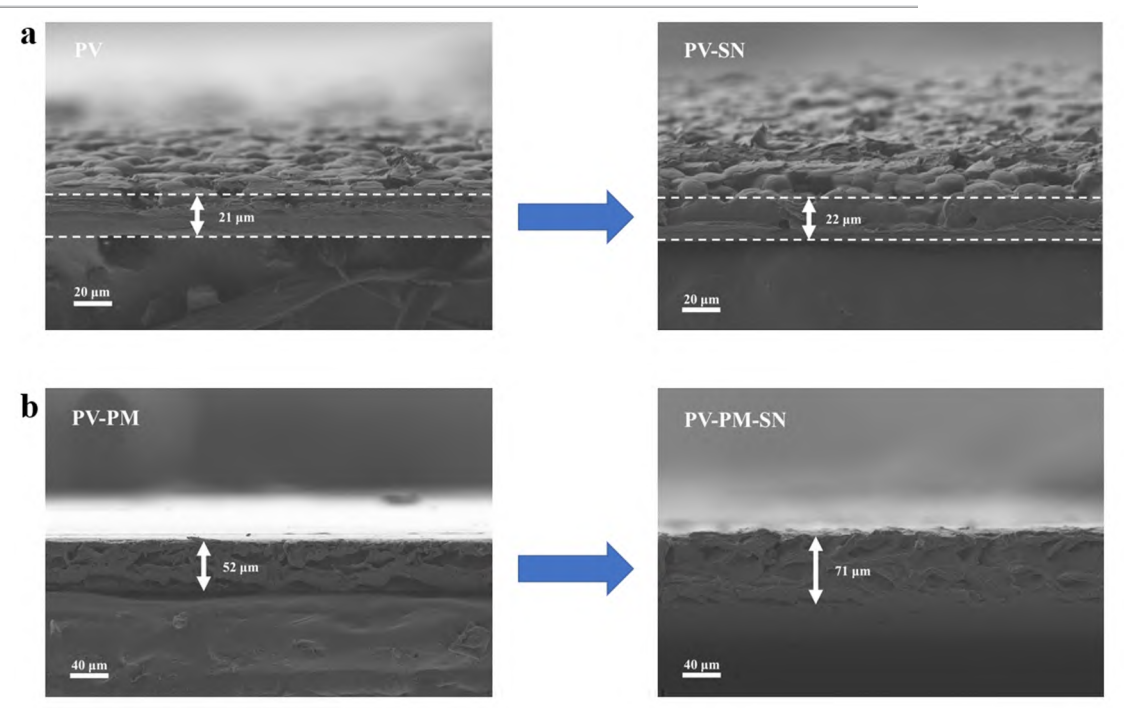


Figure S3. Cross-section view of the membranes before and after absorbing SN. (a) PV and (b) PV-PM.



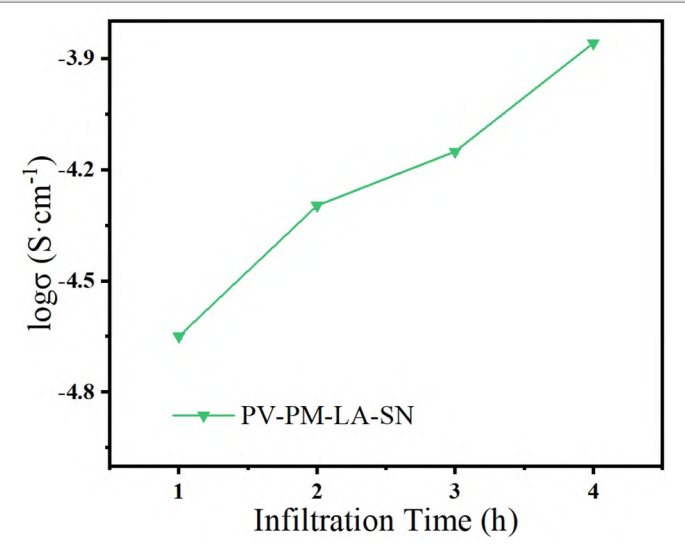


Figure S4. The relationship between the infiltration time and room-temperature ionic conductivity of PV-PM-LA-SN.



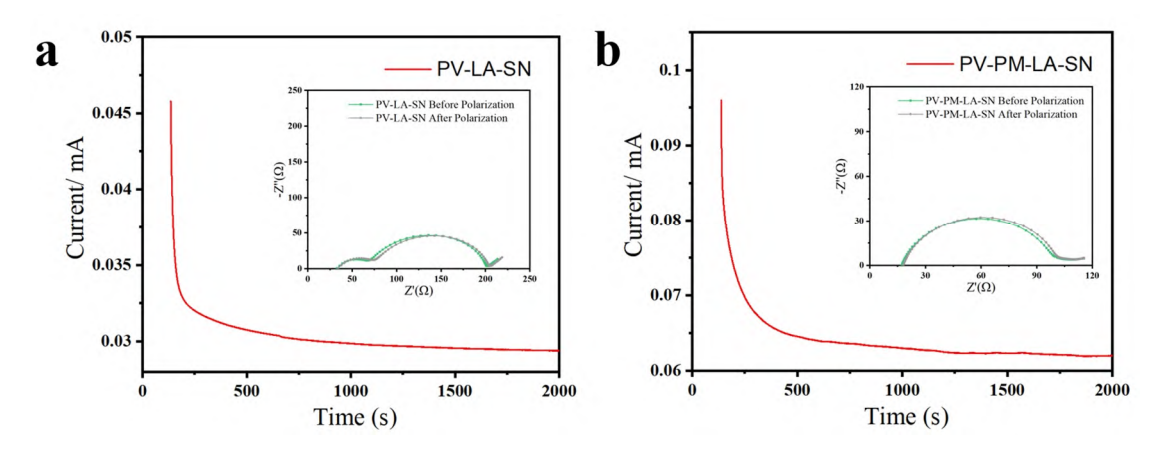


Figure S5. Polarization curve and initial and steady-state impedance diagram (the inset) for (a) PV-LA-SN and (b) PV-PM-LA-SN.



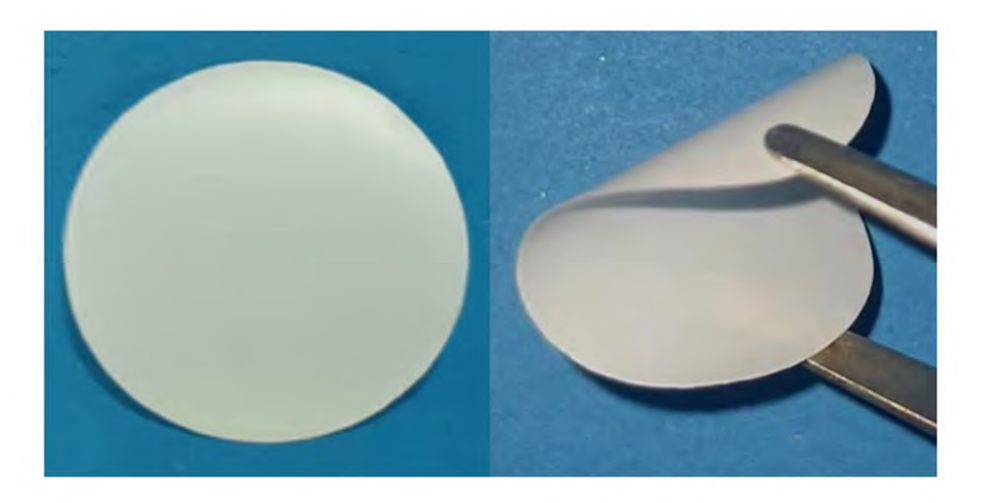


Figure S6. Photographs of PV-PM-LA membrane.



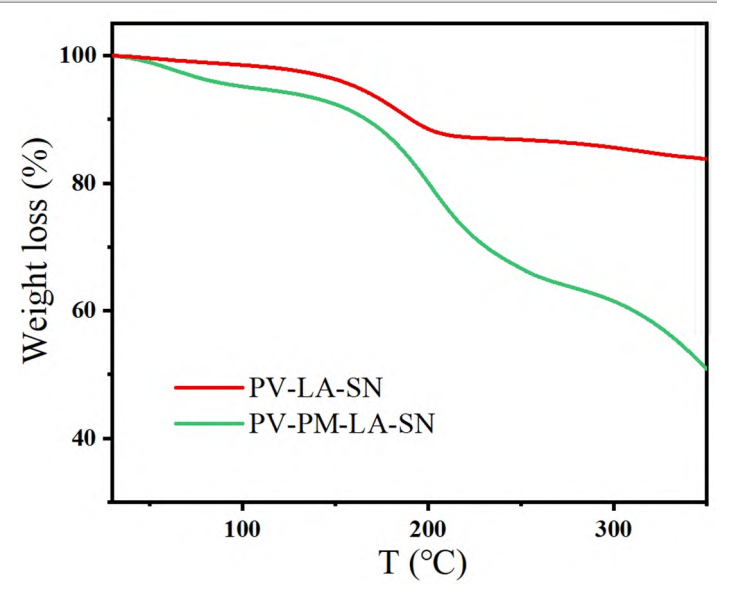


Figure S7. Thermogravimetric analysis curves of PV-LA-SN and PV-PM-LA-SN.



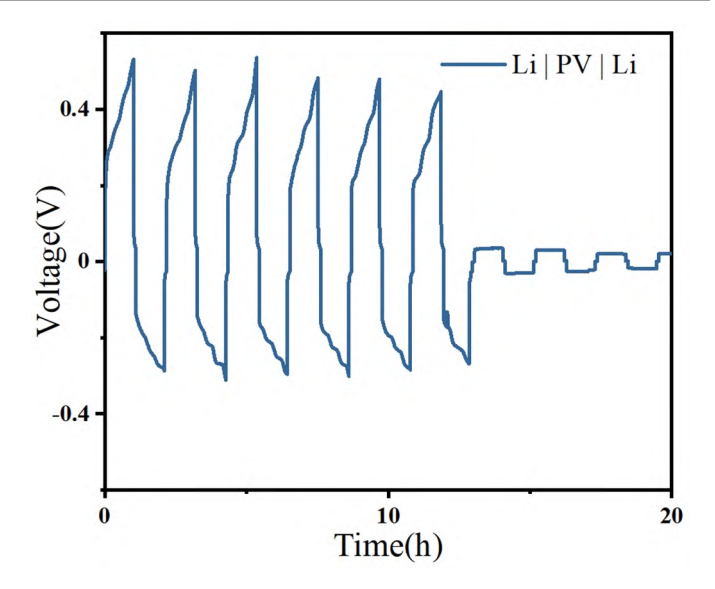


Figure S8. The voltage-time profiles of Li symmetrical cells at a current density of 0.1 mA·cm<sup>-2</sup> with a capacity of 0.1 mAh·cm<sup>-2</sup>.



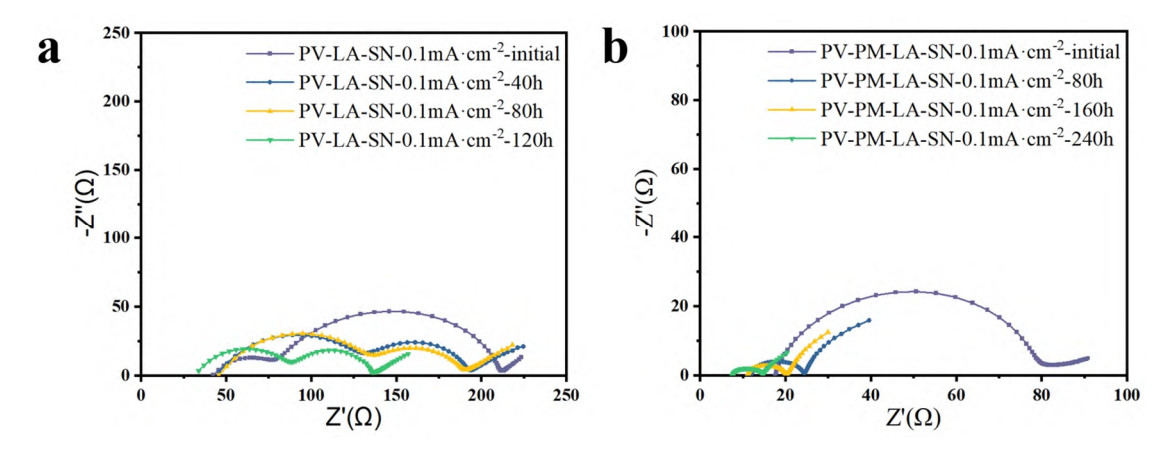


Figure S9. Nyquist plots of the symmetric Li cells measured at different cycling time for (a) PV-LA-SN and (b) PV-PM-LA-SN.



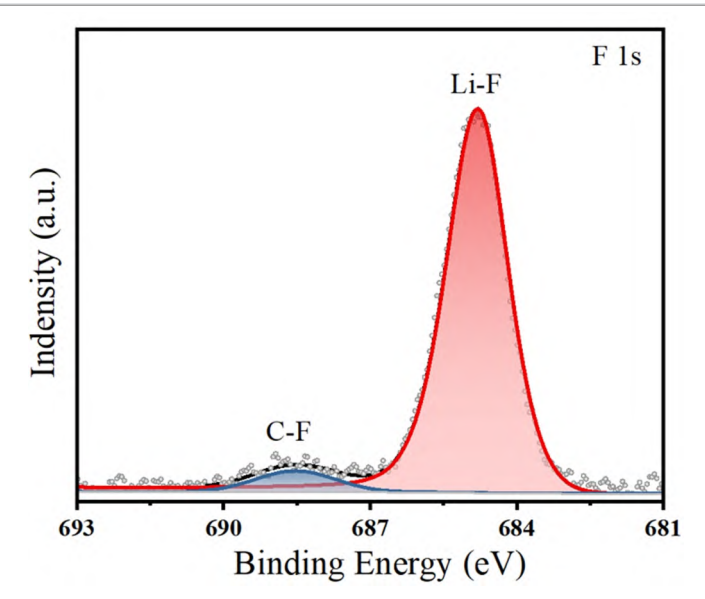


Figure S10. The X-ray photoelectron spectroscopy spectrum of the surface of Li-FEC.



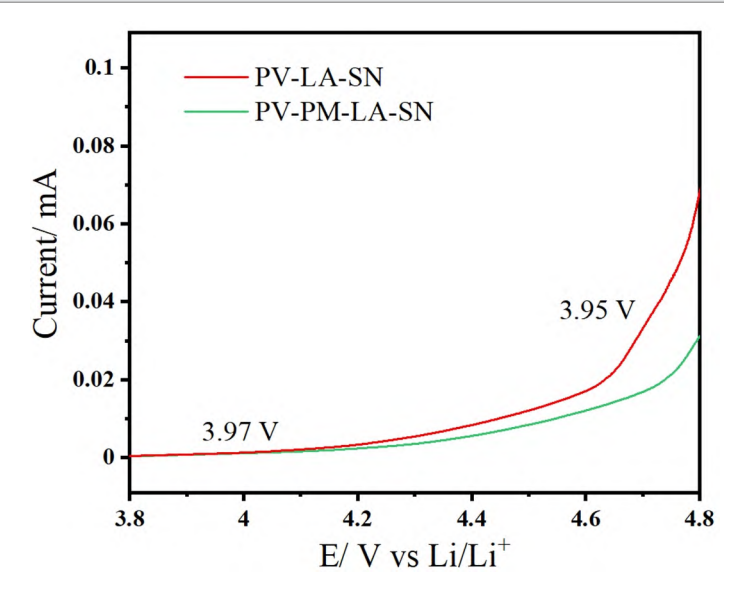


Figure S11. Linear sweep voltammetry for PV-LA-SN and PV-PM-LA-SN.



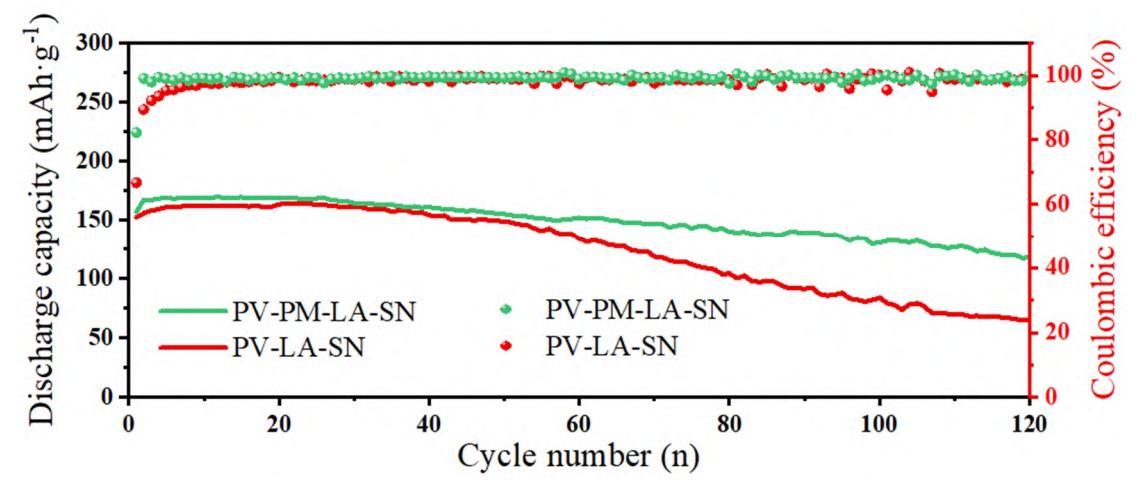


Figure S12. Discharge capacities and coulombic efficiency of Li/NMC532 cells at 0.2 C.